Wall-Modeled Large Eddy Simulations of Transonic Buffet Over a Supercritical Airfoil

Ryan D. Hass[*], Jeffrey A. Housman[†], Gerrit-Daniel Stich[‡], and Jared C. Duensing[§]
NASA Ames Research Center, Mountain View, CA, 94035

A series of scale-resolving simulations of flow over the ONERA OAT15A airfoil have been performed at an angle of attack of $3.5°$, just past the onset of buffet. The focus of this study is to document the sensitivity of the wall-modeled large eddy simulation (WMLES) methodology for curvilinear structured overset grids within the Launch, Ascent, and Vehicle Aerodynamics (LAVA) framework to mesh spacing, mesh distribution, and domain size. A secondary purpose of the study is to compare the results from WMLES to unsteady Reynolds-averaged Navier Stokes (URANS) simulations and hybrid RANS-LES (HRLES) within the same LAVA solver framework. The study provides a unique perspective regarding comparisons between different turbulence modeling approaches, time-integration methods, and computational performance since many of the same numerical routines are used for all three types of simulations. The results are compared with experiments and previous numerical studies of the same geometry and flow conditions.

I. Nomenclature

Variables:

A	=	Airfoil reference area
α	=	Angle of attack
c	=	Airfoil chord length
c_s	=	Speed of sound
f	=	Frequency [Hz]
F_D	=	Drag force
F_L	=	Lift force due to integrating the surface pressure
p	=	Pressure
ρ	=	Fluid density
t	=	Time
τ_w	=	Wall shear stress
U	=	Velocity magnitude
x_i	=	Spatial location in a Cartesian coordinate system
ξ, η, ζ	=	Streamwise, spanwise, and wall-normal directions respectively
$(\cdot)_\infty$	=	Variable value in the free-stream
$(\cdot)_{\text{RMS}}$	=	Root mean square of a variable

Nondimensional parameters:

M_∞	=	Free-stream Mach number, U_∞/c_s
Re_c	=	Reynolds number based on chord length
C_D	=	Drag coefficient, $2F_D/(\rho_\infty A U_\infty^2)$
C_f	=	Skin-friction coefficient, $2\tau_w/(\rho_\infty U_\infty^2)$
C_L	=	Lift coefficient, $2F_L/(\rho_\infty U_\infty^2 A)$

*NASA Pathways intern, Computational Aerosciences Branch, ryan.d.hass@nasa.gov.

†AST Fluid Mechanics, Computational Aerosciences Branch, jeffrey.a.housman@nasa.gov, AIAA Senior Member.

‡Senior Research Scientist, Science and Technology Corporation (STC), Computational Aerosciences Branch, gerrit-daniel.stich@nasa.gov, AIAA Senior Member

§Branch Chief, Computational Aerosciences Branch, jared.c.duensing@nasa.gov, AIAA Member.

C_p =   Pressure coefficient, $2(p - p_\infty)/(\rho_\infty U_\infty^2)$
St   =   Strouhal number, fc/U_∞

Operators:

$\langle g \rangle$ =   Mean
$\langle g \rangle_t$ =   Time average
g' =   fluctuations about the mean, i.e., $g - \langle g \rangle$

II. Introduction

Aircraft designed to operate at transonic cruise speeds (roughly $M_\infty \in [0.7, 1.2]$) may encounter what is known as "transonic shock buffet" which limits the range of the operational flight envelope. This phenomon was first identified in 1947 [1] and has since been extensively studied in the literature due to significant performance degradation and safety concerns as a result. Transonic flow occurs when the flow locally accelerates to supersonic speeds somewhere along the wing, and then returns to subsonic conditions before the trailing edge. A shock wave develops when the flow returns to a subsonic state and, depending on the Mach number and angle of attack, a separated flow region develops just downstream of the shock. Once the separated flow region becomes large enough, the shock becomes unsteady, oscillating fore and aft. The shock foot typically marks the location of boundary layer separation and as the shock moves, the size of the downstream separated flow region changes in time, thus creating significant oscillations in integrated loads such as lift and drag. These load-oscillations are at best unpleasant for passengers, and at worst, catastrophic for the structural integrity of the aircraft. As such, the buffet region must be well-defined during aircraft design and avoided during flight. Much research has been done on buffet over three-dimensional (3D) wings, which is qualitatively different from two-dimensional (2D) airfoils, especially for highly swept wing designs [2]. While 3D wing configurations are the more relevant geometries in terms of practical application, studying buffet over 2D airfoils is still a worthwhile exercise. For one, the cross-section of 3D swept wings are designed based on 2D airfoil studies and characteristics. Second, understanding buffet over a 2D airfoil is a necessary condition to the more practical 3D wing since the complicating influence of transverse flow is eliminated and the shock/boundary-layer/wake interactions can be studied in isolation. Finally, 2D scale-resolving simulation analysis is inherently less computationally expensive than 3D analysis.

Numerous numerical studies of 2D airfoil shock buffet have been done in the past (see e.g., the studies summarize in [2]). The Unsteady Reynolds-Averaged Navier-Stokes (URANS) methodology offers a compromise between computational efficiency and accuracy for simulating 2D airfoil shock buffet. In this approach, large-scale unsteady motions such as shock oscillations are directly simulated, while smaller-scale turbulent fluctuations are modeled. This allows URANS to capture key characteristics of buffet while maintaining reasonable computational costs. However, the accuracy and reliability of URANS predictions strongly depend on the chosen turbulence model and numerical discretization schemes, both spatial and temporal [3–6]. This sensitivity raises concerns about URANS results that lack experimental validation. To address these limitations, researchers have turned to large eddy simulation (LES) techniques, which directly resolve energetic turbulence scales. While LES offers potentially more general and less sensitive predictions, wall-resolved LES (WRLES) becomes computationally prohibitive at Reynolds numbers of practical interest [7]. Consequently, the choice of simulation method for buffet phenomena involves balancing computational efficiency, accuracy, and applicability to realistic flow conditions.

To circumvent this computational roadblock, various modeling strategies have been introduced to alleviate the near wall resolution and time-step restrictions imposed by the small near-wall scales. These modeling strategies can broadly be classified as hybrid RANS-LES (HRLES) and wall-modeled LES (WMLES). The former utilizes RANS equations and turbulence closures in regions where the turbulent boundary layer is attached, where RANS methods have a strong record of accuracy and are considered very reliable. In regions of significant separation and complicated flow physics (such as shock-turbulence interaction) an LES methodology is employed. While in principle this hybrid approach combines the best attributes of both solution strategies, in practice, for transonic buffet applications, solution accuracy is extremely sensitive to the RANS-LES transition location and the level of turbulence generated there [2]. It also inherits at least some of the sensitivities of the underlying RANS model, at least in attached flow regions. Nevertheless, various HRLES strategies have been employed successfully to study and predict shock buffet [8–10].

The second modeling approach, WMLES, seeks to apply the LES methodology globally, thereby avoiding altogether the complication of determining/predicting the RANS-LES handoff location. It also seeks to avoid the computational cost associated with resolving the inner-layer of the turbulent boundary layer by replacing the no-slip boundary condition

with wall-stress boundary conditions provided by the wall model. The wall model uses the near-wall LES velocity as an input and returns the appropriate wall shear stress boundary condition at each time step. One of the first successful applications of WMLES to the study of shock buffet for the ONERA OAT15A supercritical airfoil was done by Fukushima and Kawai [11]. Using a structured, curvilinear discretization, they demonstrated the predictive capability of WMLES for the problem and compared with existing URANS and HRLES strategies reported in the literature. The authors in that paper reported very good agreement with experimental data in terms of averaged surface C_p, root mean square (RMS) of surface pressure fluctuations, mean velocity profiles, and a number of other quantities. Consequently, these results, and the ability of WMLES to resolve higher frequency content, it seemed that the close correspondence with experiment was due to robustness of the method, avoiding the need for ad hoc model modifications as in the case of URANS or HRLES. However, at least two other studies of WMLES of shock buffet on the NASA Common Research Model (CRM) showed a persistent tendency to predict a shock location that was downstream of experimental measurements [12, 13]. This tendency was also observed in Tamaki and Kawai [14] using a similar WMLES methodology as applied to the ONERA OAT15A. The performance of the WMLES of Fukushima and Kawai [11] motivated us to conduct a systematic sensitivity study of the problem. We wanted to answer the following question: in terms of engineering quantities of interest (specifically, C_L, C_D, C_p, $p_{\mathbf{RMS}}$, and C_f), how sensitive are results from WMLES (of the OAT15A airfoil beyond buffet onset) to the following:
1) Mesh distribution
2) Mesh resolution
3) Spanwise and far-field extent of the computational domain
4) Choice of wall-model
5) Choice of subgrid stress (SGS) model
6) Choice of numerics

This manuscript explores items 1-3 and begins to examine item 4 by assessing the sensitivity to wall-model matching location, the location near the wall that data is provided to the wall-model. Items 5 and 6 (as well as further analysis of 1-4) is planned for the future. In addition, results are also compared with HRLES and URANS simulations using the same solver framework. The paper is organized as follows: Section III summarizes the numerical methods and turbulence models employed in our code. Section IV presents results from our WMLES for a series of numerical grids, different domain sizes including variations in spanwise extent and far-field location, and wall-model matching locations. In addition to the WMLES sensitivity studies, comparisons with URANS and HRLES simulations for a family of structured overset grids are also presented and used for comparitive purposes. Concluding remarks are provided in section V.

III. Numerical methods, turbulence modeling, and computational mesh generation

The Launch, Ascent, and Vehicle Aerodynamics (LAVA) solver framework [15] is utilized for the computational study. Specifically, we utilized the structured curvilinear solver within the framework. For WMLES, the solver applies a finite-difference formulation to solve the compressible filtered Navier-Stokes equations written in general curvilinear strong conservation law form. An ideal gas equation of state along with an appropriate sub-grid stress (SGS) model are used to close the system. A 3rd order total variation diminishing Runge-Kutta (RK3-TVD) time integration scheme [16] is used to march the unsteady equations forward in time. Furthermore, we incorporate overset grid technology [17] to couple solutions across different overlapping meshes.

A. Low dissipation finite-difference method

Low dissipation finite-difference schemes have been shown to be an accurate and efficient strategy for turbulence resolving simulations using LAVA [18–21] . A thorough study comparing several finite difference methods on Cartesian grids within the LAVA framework was reported previously [22]. More recently, [23] showed the accuracy and robustness of using Kinetic Energy and Entropy Perserving (KEEP) schemes combined with upwind-biased WENO-based artificial dissipation locally activated based on a vorticity strain rate sensor for WMLES simulations of a CRM65 swept wing at low speed conditions using the LAVA curvilinear solver. Results from these, and similar, studies have informed the current numerical formulation where the convective fluxes are evaluated using the KEEP scheme with upwind-biased WENO-based artificial dissipation activated using a combination of the aforementioned vorticity strain rate sensor combined with a local pressure-based shock-sensor. The non-dissipative portion of the flux remains second-order accurate while the dissipative portion of the flux is third-order but only activated across shocks or regions where the

strain rate magnitude is significantly larger than the vorticity magnitude. Explicit RK3-TVD [16] is used for physical time-integration with a CFL number of 1.5.

B. Turbulence modeling - RANS, SGS, and wall models

While not the focus of this paper, we do present results from a series of URANS and HRLES computations performed on the same case, so a brief description of the turbulence models used in those simulations is provided. The URANS equations are closed with the Spalart-Allmaras (SA) turbulence model including a compressibility correction [24]. For HRLES the Zonal Detached Eddy Simulation (ZDES) mode 2 (2020) [25] is used with the same SA-CC turbulence model to close the system (note, after discussing some of the results with the original authors of the model they suggested to turn-off the compressibility correction, and this was not done for the results in this paper but will be applied in future work). A similar low-dissipative convective flux discretization is utilized for both the URANS and HRLES simulations, but instead of the KEEP scheme, a modified Roe-HLL scheme [26] is utilized where the left and right states to the flux are blended between 3rd order upwind-biased WENO and 4th order centered interpolations based on the vorticity strain rate sensor and the flux locally switches from the Roe flux to the HLL flux across shocks.

For the WMLES, an anisotropic form of the Vreman SGS model is used a with constant coefficient $C_{SGS} = 0.07$. For the near wall region, we impose the stress from the wall-model through the viscous flux [27–29] which have proven successful in other applications within the LAVA framework [23, 30–33]. The stress-based WMLES approach computes the LES solution all the way to the wall using wall stress and heat flux boundary conditions provided by the wall model [33]. The wall model, in turn, uses the LES solution near the wall as input. The schematic diagram in Fig. (1) illustrates the key principles of the WMLES approach used. An algebraic equilibrium wall function, typically taking information from the second off-wall solution node as input, is employed as the wall model. The implemented algebraic wall model is an analytical law that smoothly blends the viscous sub-layer and log-layer [33]. It is important to note that WMLES relies on a global LES closure of the flow-field. Additional details regarding the WMLES approach in LAVA can be found in [23, 33, 34].

In order to ensure the flow transitions from laminar to turbulent at the same location as imposed in the experiment, we implemented a slip-wall boundary condition before encountering a trip strip at $x/c = 0.07$ on both the upper and lower surface. We change the boundary condition to use the wall model at this location. The tripping is implemented as physical protrusions in the geometry (cylindrical posts) which are treated via an immersed-boundary method implemented as a source term momentum penalty in the governing equations. We should note that this is a different procedure than in Fukushima and Kawai [11] where they utilized a wall-model on the entire airfoil surface, but set the eddy viscosity to zero before the trip location.
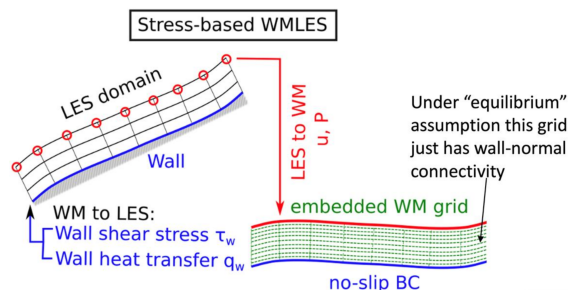

Fig. 1   Schematic showing the working principles of the WMLES method used [34].

C. Computational mesh generation

Structured curvilinear overset grids were generated using a combination of Pointwise^{TM} [35] and Chimera Grid Tools (CGT) [36]. Table 1 provides details of each mesh used in the analysis. The HRLES and URANS meshes are based on findings published in Deck et al. [25] as well as our internal study of a 2D version of the OAT15A airfoil as published in Maldonado et al. [37] and previous studies utilizing URANS [38, 39]. Both the URANS and HRLES-based meshes belong to the family of RANS-Based (RB) meshes where the cells near the wall are clustered to achieve y-plus values of less than one, resulting in high-aspect ratio, strongly skewed cells. This necessitates the use of more expensive implicit-time marching schemes due to the time-step restrictions of explicit schemes. Three different URANS meshes

Table 1   Mesh and domain parameters for all simulations discussed in this paper. Where ξ, η, and ζ are the streamwise, spanwise, and wall-normal directions.

| Simulation type	Mesh family	ID	$\Delta\xi_{min}/c$ ($\times 10^{-6}$)	$\Delta\eta/c$ ($\times 10^{-6}$)	# Points in η	$\Delta\zeta_{min}/c$ ($\times 10^{-6}$)	Total node count (million)	Spanwise extent (relative)	Farfield extent
URANS	RB	U1	1,049	10,417	25	5.37	7.543	$0.25c$	$164c$
URANS	RB	U2	1,049	5,000	50	5.37	15.387	$0.25c$	$164c$
URANS	RB	U3	1,049	2,500	100	5.37	30.472	$0.25c$	$164c$
HRLES	RB	H1	Same as U1						
HRLES	RB	H2	Same as U2						
HRLES	RB	H3	Same as U3						
HRLES	RB	H4	1,049	1,250	200	5.37	60.642	$0.25c$	$164c$
HRLES	RB	H3b	1,049	2,500	100	5.37	32.043	$0.25c$	$164c$
HRLES	RB	H4b	1,049	1,250	200	5.37	71.876	$0.25c$	$164c$
WMLES	A	WM_A	110	115	566	140	227.200	$0.065c$	$80c$
WMLES	B	WM_FK	113	115	282	116	439.468	$0.065c$	$80c$
WMLES	B	WM_B1	113	115	566	115	446.734	$0.065c$	$80c$
WMLES	B	WM_B2	113	231	282	230	234.590	$0.065c$	$80c$
WMLES	B	WM_B3	238	231	282	230	200.581	$0.065c$	$80c$
WMLES	B	WM_B4	238	231	282	230	159.716	$0.065c$	$80c$
WMLES	B	WM_B5	113	231	282	230	293.167	$0.065c$	$80c$
WMLES	B	WM_B2f2	113	231	282	230	242.391	$0.065c$	$200c$
WMLES	B	WM_B2s2	113	231	563	230	469.180	$0.13c$	$80c$
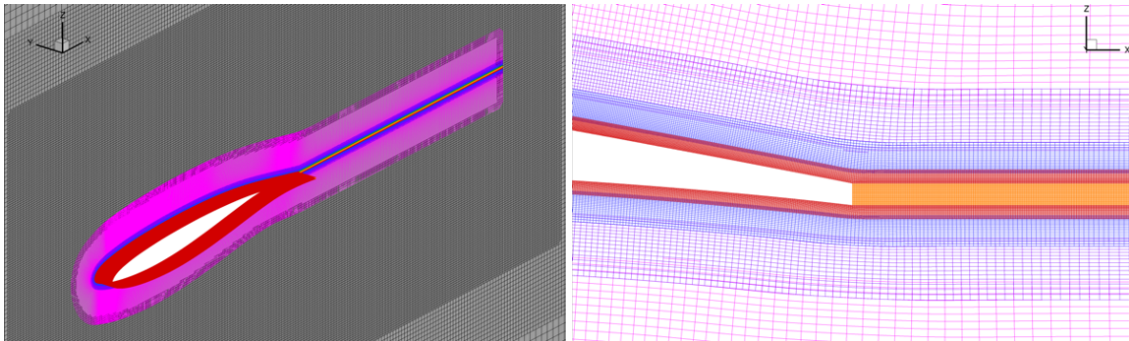
Fig. 2   Depiction of multi-layer mesh growth strategy utilized in type A mesh (WM_A). The streamwise and spanwise spacings are reduced by a factor of 2 in each subsequent layer away from the wall.

(U1, U2, U3) were utilized in this study. The major difference among these three meshes is in the spanwise resolution, as shown in Table 1, ranging from 25 to 100 uniformly spaced points. In total, six HRLES meshes were generated, where meshes H1-H3 are consistent with the URANS meshes. The spanwise number of mesh points was doubled one additional time in HRLES to 200 points, resulting in mesh H4. Furthermore, two additional meshes were generated (H3b and H4b) to add streamwise refinement in an attempt to improve grid aspect ratios in the post-shock separated flow region where the model utilizes LES.

The major focus of this paper is on scale-resolving simulations using WMLES. A significant advantage of the WMLES-type meshes is that they relax the stringent y-plus requirement, resulting in more isotropic cells near the wall. This approach enables a more efficient resolution of turbulent structures across a wider range of scales. For the WMLES study, we developed two mesh distribution types, designated as "Type A" and "Type B". Type A is based on developed best-practice guidelines for aerodynamic applications, as utilized in previous studies such as the High-Lift Common Research Model [40] as well as jet noise simulations [41]. These mesh types are specifically designed to optimize the balance between computational efficiency and accuracy in capturing the complex flow physics inherent in scale-resolving simulations. For the Type A mesh, a multi-layer volume growing technique was employed to reduce the overall mesh count and cell aspect ratios away from the surface. This technique is illustrated in Fig. (2), where we color-coded the first layer in red, the second in blue, and the third in purple. In each layer, we halved the number of points in both the streamwise and spanwise directions. This grid-generation method was previously established as a best practice when generating grids for complex geometries such as the NASA Common Research Model (CRM) and its high-lift variant (CRM-HL) [12, 34]. Generating the mesh in this way preserves the fine near-wall spacing used in Fukushima and Kawai [11], which was informed by boundary layer thickness estimates as established in [28], while reducing the global cell count by a factor of two. However, this approach has shown to be disadvantageous for the prediction of buffet, as the shock extends significantly beyond the near-wall region and requires finer resolution (specifically in the streamwise direction) away from the wall. When comparing the Type A mesh with experiments, we observed significant differences which were not seen in the WMLES of Kawai et al. [42]. The major difference between Kawai's WM_FK mesh and our WM_A mesh lies in the use of the previously described multi-layer grow-out region. As a result of these differences, we communicated with Kawai's team, who graciously supplied us with the
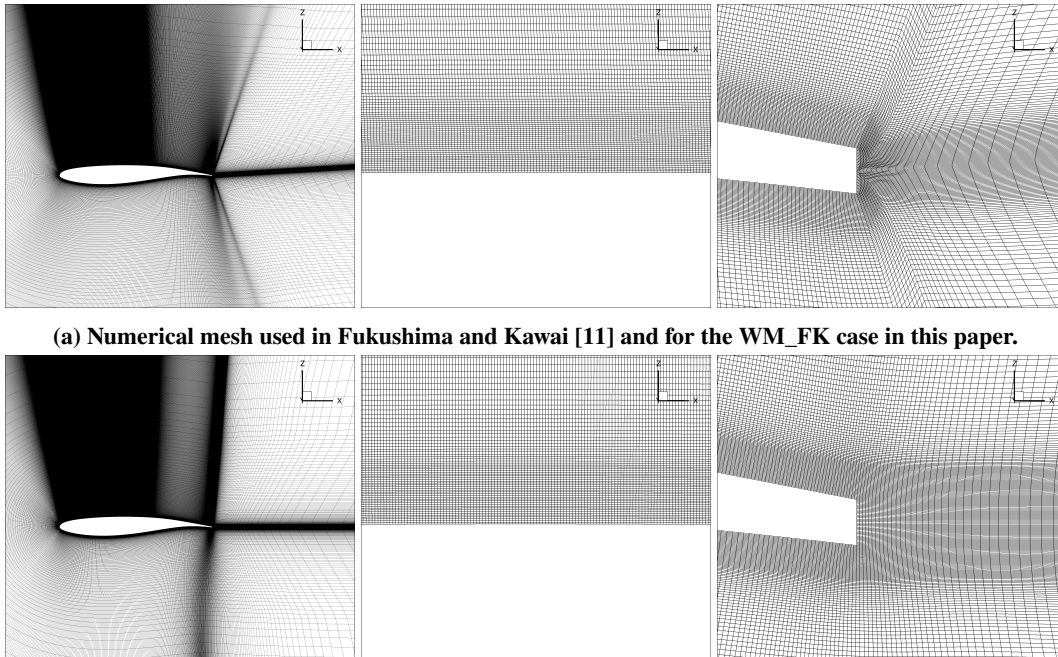
(a) Numerical mesh used in Fukushima and Kawai [11] and for the WM_FK case in this paper.

(b) WM_B1: Identical surface and wall-normal resolution, applied modification in TE of airfoil to improve cell quality.

Fig. 3   Trailing edge modification to the mesh in [11]. The center column of figures is zoomed in on the suction side near $x/c = 0.5$.

6

(a) WM_B1 streamwise spacing

(b) WM_B1 wall-normal spacing

(c) streamwise difference WM_B1 and WM_B2

(d) streamwise difference WM_B1 and WM_B3

(e) streamwise difference WM_B1 and WM_B4

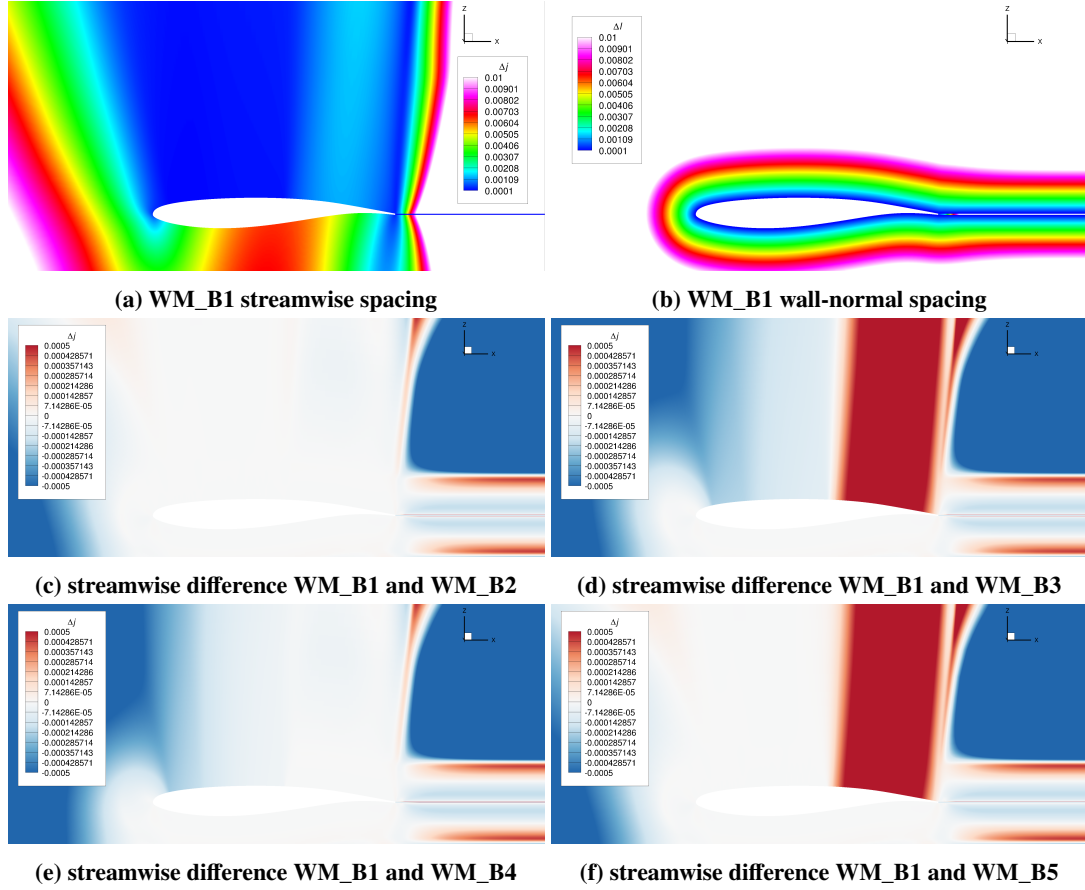**(f) streamwise difference WM_B1 and WM_B5**

Fig. 4   Streamwise (a) and wall-normal (b) mesh spacings for the Type B WMLES meshes. (c)-(f) Difference in streamwise spacing between baseline WM_B1 and subsequent modified meshes. Red indicates refinement compared with baseline mesh, blue indicates coarsening.

mesh they utilized in their study. This enabled a better comparison between the WMLES approaches while minimizing grid effects on the simulation data. We made only minimal modifications to this mesh, limited to the treatment of the trailing edge mesh to improve overall cell quality in the wake mesh. This modified mesh, which aims to keep mesh spacings consistent across the whole airfoil, is labeled as mesh WM_B1 and is depicted alongside the unmodified mesh in Fig. (3). We did not observe any qualitative differences in the simulations between Kawai's original grid and our modified TE grid. However, due to the utilization of explicit time-stepping, our modified version of the mesh resulted in a larger time-step size and thus a reduction of overall simulation cost. Due to the Type B mesh's superior agreement with experimental results, we focused our mesh resolution study on this distribution. Five different meshes were examined, systematically varying: spanwise and wall-normal spacing (WM_B1 & WM_B2), leading-edge streamwise spacing (WM_B3 & WM_B4) and trailing-edge streamwise spacing (WM_B3 & WM_B5).

While these near-wall spacings affect off-body mesh characteristics, we primarily discuss them in terms of surface mesh distribution and resolution. Figure (4) provides a visual and quantitative comparisons of the mesh differences. Figure (5) displays a global view of the general mesh as well as quantitative surface mesh spacings in both streamwise (Δj), spanwise (Δk) as well as wall-normal (Δl) direction along the airfoil suction side. Finally, Fig. (6) shows the wall-normal as well as streamwise mesh spacings along four profiles normal to the wall (x/c=0.1, 0.25, 0.5 and 0.75).

Finally, we conducted sensitivity studies to determine the domain size sensitivity for the far-field distance (WM_B2f2) and sensitivity to the spanwise extent of the domain (WM_B2s2). For these studies, mesh WM_B2 was chosen as a baseline to minimize computational costs. For the domain size sensitivity study, we extended the far-field distance from 80 chord lengths to 200 chord lengths. The final study tested the influence of the spanwise extent, where we doubled the domain size from $0.065c$ to $0.13c$ while keeping the spacing in the spanwise direction constant.
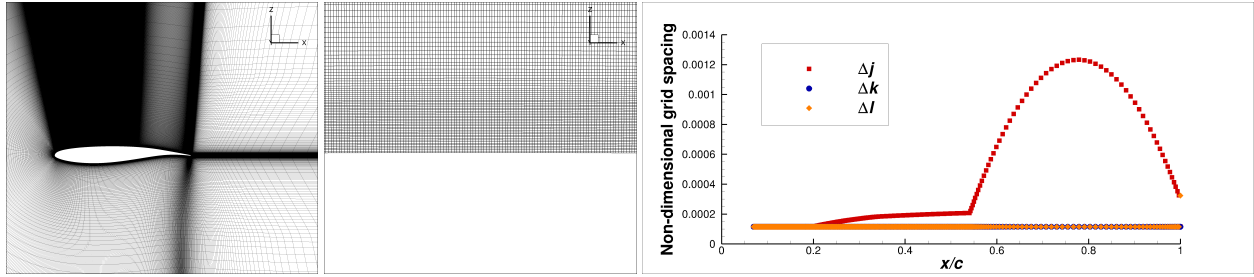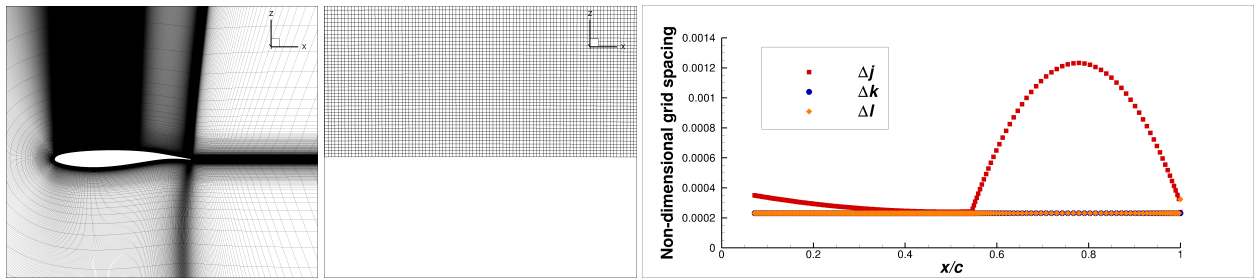
(a) WM_B1: Identical surface and wall-normal resolution as [11] with applied modification in TE of airfoil to improve cell quality.
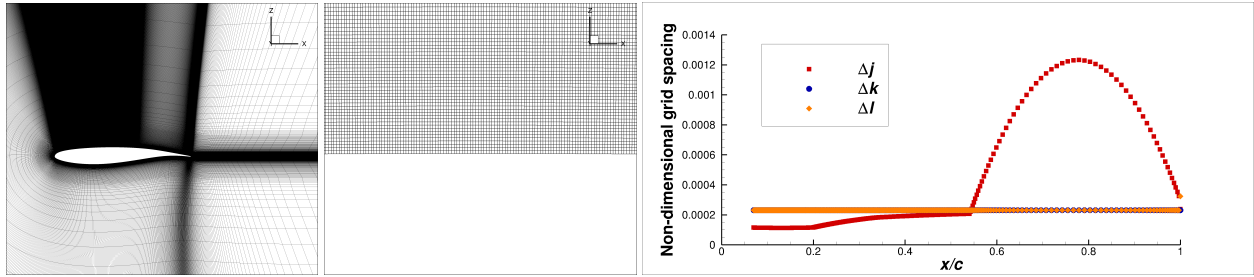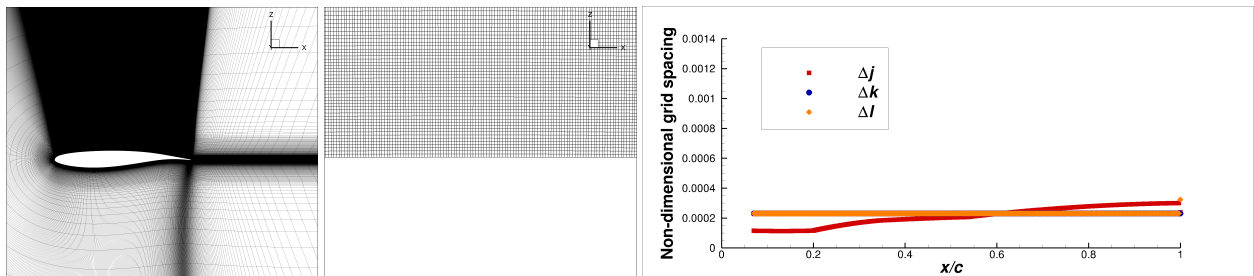

(b) WM_B2: Coarsening in spanwise and wall-normal spacings. Streamwise spacing consistent with WM_B1
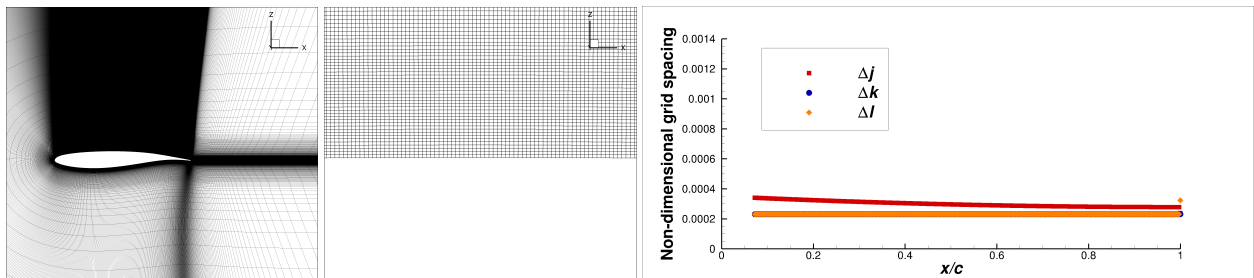
(c) WM_B3: Spanwise and wall-normal same as WM_B2, re-distribution and coarsening of streamwise spacing.

(d) WM_B4: Spanwise and wall-normal same as WM_B2, added parabolic profile of WM_B1 in downstream region.

(e) WM_B5: Spanwise and wall-normal same as WM_B2, Streamwise spacing modifed to remove parabola in downstream region.

Fig. 5   Five mesh resolutions for the Type B distribution. The center column of figures is zoomed in on the suction side near $x/c = 0.5$. The right column shows surface mesh spacings. Δj, Δk, and Δl correspond to the streamwise, spanwise, and wall-normal mesh spacing.

(a) x/c=0.1 **(b)** x/c=0.25 **(c)** x/c=0.5 **(d)** x/c=0.75
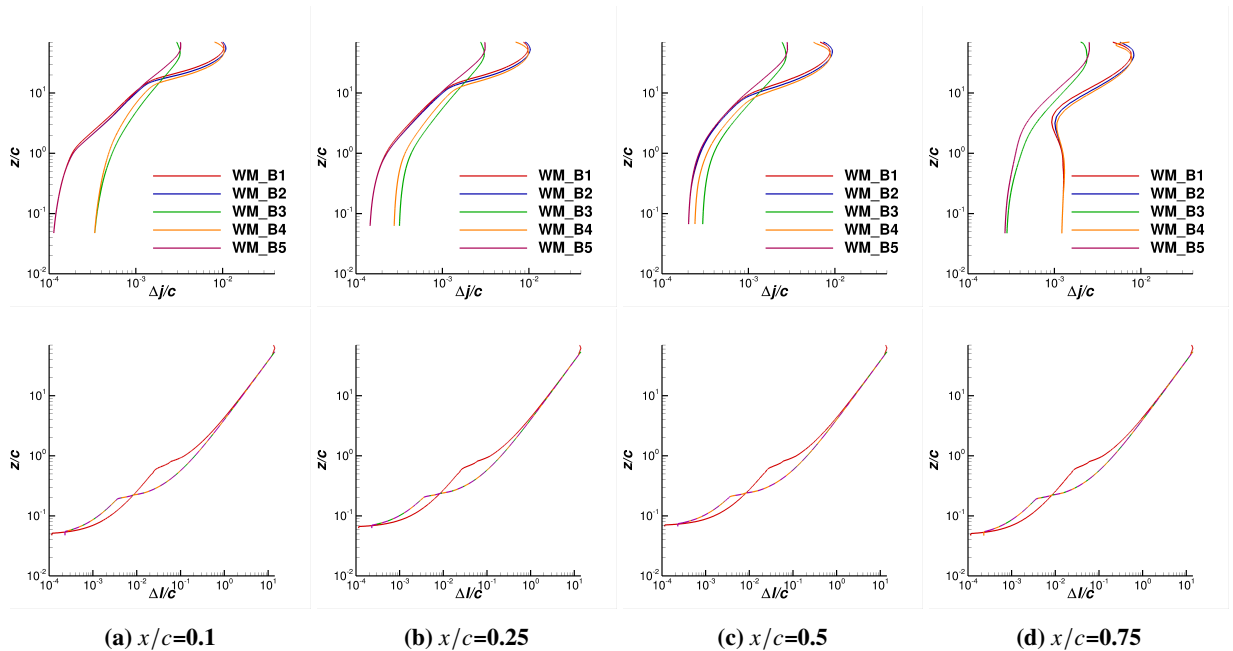
Fig. 6   streamwise and wall-normal mesh spacings for the Type B WMLES runs. WM_B2, WM_B3, WM_B4, and WM_B5 have the same wall-normal spacing which is why only two curves are visibly in the bottom row of figures. To emphasize this, we used dashed lines on the bottom row figures with corresponding colors to the legends in the top row.

IV. Results

The OAT15A airfoil, developed by ONERA, is a supercritical airfoil designed for transonic flow conditions [43]. It has been the subject of numerous experimental and numerical studies due to its importance in understanding complex transonic flow phenomena, particularly shock buffet [2, 8, 11, 44]. One of the key challenges in studying the OAT15A airfoil is accurately predicting and analyzing the self-sustained shock wave oscillations that occur under certain transonic conditions. The results presented in this paper focus on simulations of the ONERA OAT15A airfoil at a free stream Mach number, $M_\infty = 0.73$; Reynolds number based on chord length and free stream velocity, $Re_c = 3 \times 10^6$; and angle of attack, $\alpha = 3.5°$. These conditions are just past the buffet onset condition as determined by experiment [43]. The chord length of the OAT15A airfoil is 9 inches (approximately 228.6 mm) as used in the experiments conducted in the ONERA S3Ch wind tunnel. Statistics are averaged in span and time unless otherwise specified, with a standardized averaging window of 115 convective time units (CTUs) for each case, corresponding to about 7.5 buffet cycles. The only exception is case WM_B2s2, which, due to resource constraints, was integrated for about 39 CTUs, or roughly 2.5 buffet cycles. Though, we note that this is comparable to the averaging window used in [11] which was 30 CTUs.

Our investigation into the OAT15A airfoil was motivated by previous attempts to simulate shock-buffet problems within our group. Initial simulations using a Type A mesh, which preserved the minimum near-wall spacing reported in [11], yielded results that deviated significantly from published literature, particularly in predicting mean shock location and oscillation amplitude. This led us to hypothesize that the mesh was the primary factor affecting the results.

To remove these meshing discrepancies and enable a better comparison with results from Fukushima [11], Dr. Soshi Kawai generously provided his mesh as described in Section III.C. Despite using the same mesh, the results revealed discrepancies between our LAVA solver results and the published data by Fukushima. The averaged surface C_p and pressure RMS are shown in Fig. (7), clearly showing a discrepancy between the published results and those obtained with LAVA using the current solver options. Most notably, the shock is predicted too far downstream compared to experiment and the $p_{\mathbf{RMS}}$ indicates the shock traversal region is too narrow and shifted towards the trailing edge. Although some better agreement in post-shock $p_{\mathbf{RMS}}$ is observed in the LAVA solution. This indicated that other factors, such as the wall-model, SGS model, numerical discretization, boundary conditions, and matching location, might be contributing to the differences.

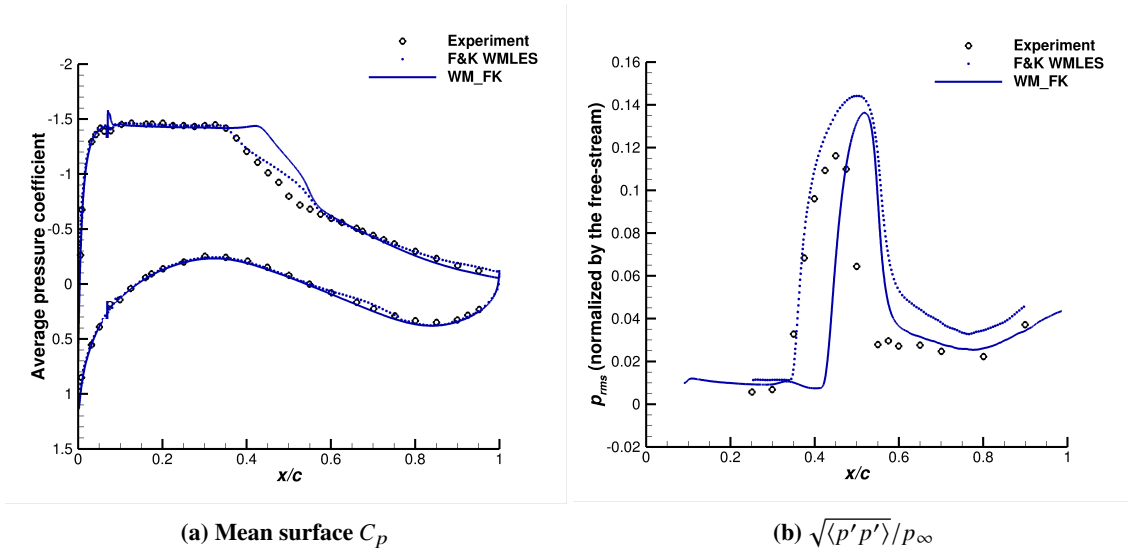In the following sections, we present our systematic study of mesh variations and their impact on the prediction of

(a) Mean surface C_P (b) $\sqrt{\langle p'p'\rangle}/p_\infty$

Fig. 7 Comparison of surface pressure using the same mesh from [11]. "WM_FK" denotes the WMLES using the LAVA software with the mesh from [11].

shock buffet and overall flow characteristics. We also briefly examine the effect of the wall-model matching location, which serves as a starting point for identifying potential reasons for the observed discrepancies. This ongoing work contributes to the broader understanding of complex flow physics in transonic conditions. It is important to note that this work is still ongoing, and further investigation is planned to address the remaining discrepancies and improve our understanding of transonic buffet. Additionally, we have two other publications investigating transonic buffet for both a 2D version of the OAT15A and the Transonic Truss-Braced Wing (TTBW) aircraft configuration using URANS [37] and HRLES (TTBW only) [45], which provide further insights into this complex aerodynamic phenomenon.

A. Mesh-distribution and resolution study

Our initial investigation into mesh resolution guidelines focused on the sensitivity to off-wall mesh refinement in the shock buffeting region. The Type A mesh distribution, which rapidly coarsens streamwise and spanwise mesh spacings away from the airfoil surface, proved insufficient in simulating the OAT15A airfoil beyond the shock-buffet condition. This is evident in the surface C_p and $p_{\mathbf{RMS}}$ results: the shock location is predicted downstream of experimental observations, and the level of pressure fluctuations is drastically reduced (see Fig. (8)). In contrast, the Type B mesh, which maintains finer resolution in the off-body region, shows significant improvement in both shock location prediction and the intensity of surface pressure fluctuations. The Type A mesh's rapid coarsening leads to an under-prediction of the shock oscillation amplitude, as evidenced by the narrow "spike" in surface $p_{\mathbf{RMS}}$ and the low-amplitude oscillations in the lift signal (Fig. (9)). By increasing the resolution in the off-body shock region with the Type B mesh, we recover oscillation amplitudes comparable to other turbulence modeling strategies and the WMLES results obtained on the WM_FK mesh. This refinement also results in improved shock location prediction. These findings highlight the critical importance of maintaining adequate mesh resolution in the off-body shock region for accurate simulation of transonic buffet phenomena.

To quantify these observations, we define the width of the shock region as the distance over which the surface $p_{\mathbf{RMS}}$ is above 40% of its maximum value (which effectively removes the plateau region post-shock) and the mean shock location as the location of the peak in the surface $p_{\mathbf{RMS}}$. By fitting a cubic spline to the experimental data, we can compute these metrics and compare them across different simulations. Table (2) summarizes this comparison for the mesh distribution study. Both the Type A and Type B meshes predict a shock location that is downstream of the experimental data by nearly 6% of the chord length. Notably, the width of the shock region for WM_B1 closely matches the experimental results, indicating that the shock motion is being accurately reproduced, albeit at a location that is too far downstream. In contrast, the Type A mesh significantly suppresses the shock motion, resulting in a shock region width that is $0.1c$ smaller than the experimental value. These results underscore the critical importance of off-body mesh resolution in accurately predicting shock motion and surface pressure. When the mesh coarsens too rapidly away

10

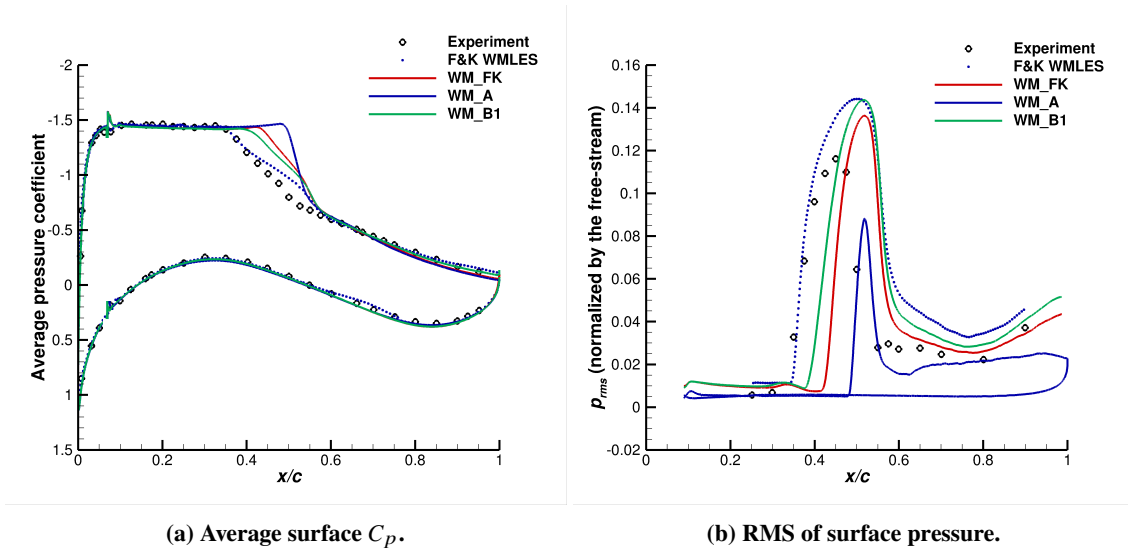(a) Average surface C_p.

(b) RMS of surface pressure.

Fig. 8 Surface pressure comparison for the Type A (WM_A) and Type B meshes (WM_B1). Overlayed for reference are the experimental values, the WMLES of [11], and the WMLES from our solver using the same mesh as [11] (WM_FK).
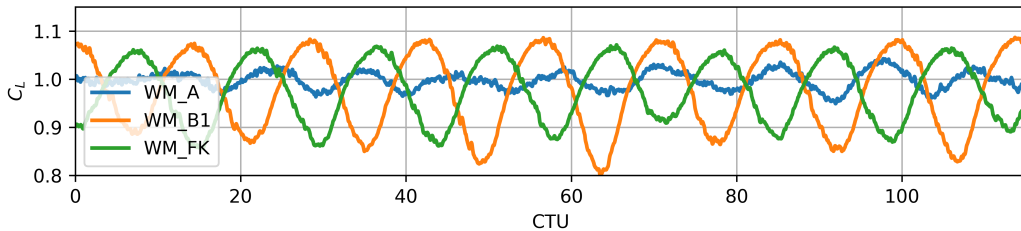

**Fig. 9   Time-history of $C_L(t)$ for WM_A, WM_B1, and WM_FK.**

from the airfoil surface, the shock becomes smeared, and its streamwise motion is drastically reduced.

An alternative view of the relative shock motion can be gleaned by quantifying the mean and RMS of lift and drag giving alternative metrics for the mean shock location and the amplitude of its oscillation respectively. These quantities are also reported in Table (2).While we do not have experimental data to compare against, these are useful metrics to conduct an internal comparison between the simulations. The significant reduction in the RMS of lift (and drag) between WM_A and WM_B1 ($C_{L,\mathbf{RMS}}$ from WM_A is 78.1% smaller than WM_B1) corroborates the conclusion that shock motion is much smaller when the off-body mesh coarsens too fast in the shock region. We also computed the frequency of the dominant mode in the lift signal and compared it to the buffet frequency reported in [43] which is calculated from a surface pressure probe at $x/c = 0.45$ as 0.0626. The Type B mesh predicts a buffet frequency slightly higher (0.0692 ± 0.0038) though, given the frequency resolution of our WMLES and the fact that the spectral peak associated with point pressure measurements may not correspond exactly to that computed from integrated lift, the Type B result is reasonable. Conversely, the buffet frequency computed from the Type A mesh is far too high (0.0773 ± 0.0043), consistent with the narrower region over which the shock moves.

As demonstrated earlier, the Type B mesh distribution, with its increased streamwise resolution in the off-body shock region, significantly outperforms the Type A distribution in terms of shock characteristics and integrated loads. To ensure consistency and further refine our understanding, we now examine five different mesh modifications within the Type B distribution family. The details of these meshes are summarized in Table (1), with a qualitative comparison provided in Fig. (5). An initial examination of the surface pressure distribution reveals sensitivity to mesh resolution, although the qualitative trends remain consistent across the different meshes. To quantify the relative agreement with experimental data, we fit a cubic spline through the suction-side experimental data and compute the root mean square

11

Table 2 Characterization of the shock location and motion. The shock width and mean location are determined from the RMS of surface pressure and the reported values are the amount above or below the experimental values of 0.1518 and 0.4595 (shock width and location respectively), e.g. quantities in blue show shock regions that are *wider* than the experiment and *further* downstream. The buffet frequency for our WMLES is computed from the lift signal whereas the value recorded for the experiment is that reported in [43] for pressure probe data at $x/c = 0.45$. The buffet frequency for F&K WMLES was determined by digitizing the spectral peak in Fig. (15) of [11] which corresponds to the pressure signal at $x/c = 0.9$.

Case	Width of shock region (difference)	Mean shock location (difference)	$\langle C_L \rangle_t$	$C_{L,\mathbf{RMS}}$	$\langle C_D \rangle_t$	$C_{D,\mathbf{RMS}}$	Buffet frequency (St)
Experiment	0	0	-	-	-	-	0.0626
F&K WMLES	0.0720c	0.0435c	-	-	-	-	0.0644
WM_A	-0.1006c	0.0584c	0.9972	0.0180	0.0459	0.0020	0.0773 ± 0.0043
WM_B1	0.0084c	0.0590c	0.9762	0.0822	0.0471	0.0072	0.0692 ± 0.0038
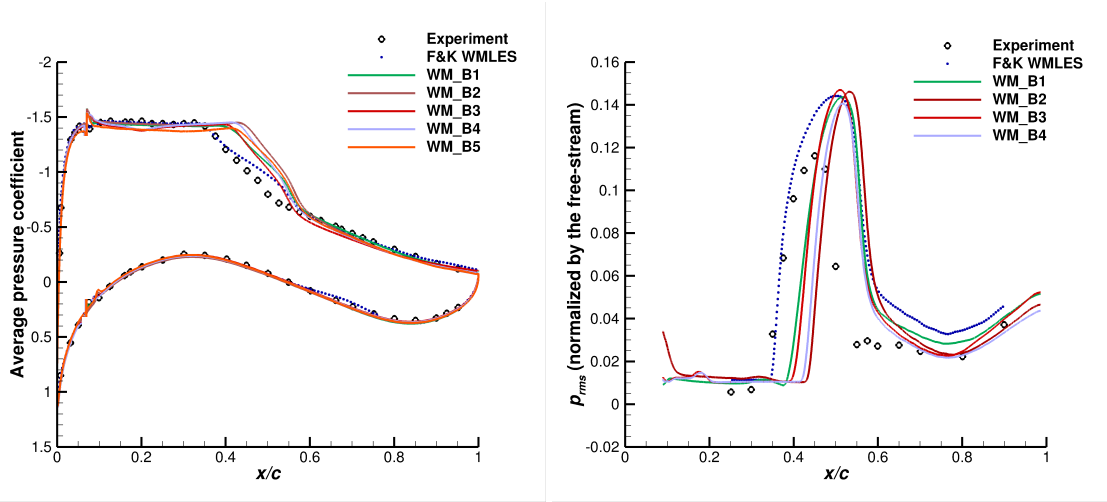
(a) Average surface C_p.

(b) RMS of surface pressure.

Fig. 10 Surface pressure comparison between the Type B mesh resolutions.

error (RMSE) of the average C_p and $p_{\mathbf{RMS}}$ in three distinct regions: Pre-shock region ($0.12 < x/c \leq 0.325$), Shock region ($0.325 < x/c \leq 0.6$), and Post-shock region ($0.6 < x/c < 0.95$).

In the pre-shock region, WM_B2 has the lowest RMSE followed closely behind by WM_B1. This is an unintuitive result considering WM_B1 is considerably higher resolution in the wall-normal and spanwise directions. Furthermore, WM_B5 has the largest RMSE at 0.0657, despite its finer streamwise resolution compared to WM_B3. We suspect these seemingly unintuitive results are due to skewed cells off the airfoil surface as a result of the modified near-wall mesh spacing, but further investigation is required to say anything definitive.

In the separated boundary layer region ($0.6 < x/c \leq 1$) WM_B1 performs the best with RMSE of 0.0112, suggesting that resolution in span and wall-normal is more critical here than in the streamwise direction. Though, the other cases are quite close to the experimental data as well, with the one notable exception being WM_B3 just behind the shock, resulting in the highest RMSE of 0.0434. In terms of turbulence content, the $p_{\mathbf{RMS}}$ post-shock for all Type B meshes is comparable to the experiment and better than the WMLES of [11] which is likely due to the improved cell-quality at the airfoil trailing edge (Fig. (3)) mentioned previously (note, we do not have $p_{\mathbf{RMS}}$ data for WM_B5 at the time of this writing).

The RMSE of C_p in the shock region itself is between 0.1701 (WM_B3) and 0.2721 (WM_B2), all of which are considerably larger than 0.0696, the RSME of the WMLES of [11]. Though, the shock motion itself is better captured

Table 3   RMSE of the suction-side surface pressure relative to the experimental data.

Case	Average C_P			Surface $p_{\textbf{RMS}}$		
	pre-shock	post-shock	shock region	pre-shock	post-shock	shock region
F&K WMLES	0.0007	0.0022	0.0696	0.0038	0.0138	0.0367
WM_B1	0.0219	0.0112	0.1905	0.0030	0.0082	0.0581
WM_B2	0.0139	0.0281	0.2721	0.0050	0.0069	0.0730
WM_B3	0.0483	0.0434	0.1701	0.0033	0.0052	0.0590
WM_B4	0.0409	0.0339	0.2257	0.0033	0.0037	0.0634
WM_B5	0.0657	0.0322	0.2207	-	-	-

by all Type B resolutions (compared to [11]) as measured by the surface $p_{\textbf{RMS}}$ which is reported in Table (4). The tendency for WMLES to predict a shock location downstream of the experiment is made explicitly clear in Table (4) as the closest agreement is $0.0519c$ downstream of the experimental value (WM_B3). An interesting observation is the relatively large buffet frequency (as computed from $C_L(t)$) for WM_B3 and WM_B5, which are the two cases with much finer streamwise spacing in the post-shock region. Why increased resolution in this area is accompanied by an increase in the shock oscillation frequency is still under investigation, but it may be related to increased cell aspect ratios off the airfoil surface due to streamwise refinement.

The friction coefficient along the suction side is shown in Fig. (11). The coarser resolutions underpredict this quantity near the leading edge as compared to the high resolution cases. This is expected since the thin leading-edge boundary layer is severely under-resolved with the wall-model matching location well outside the log layer as discussed in detail by [12]. Prior to the shock region, WM_B1 does the best job matching the WMLES results of [11] suggesting that spanwise and wall-normal resolution affects this quantity. Instantaneous contours of C_{fx} are shown in Fig. (12) to give a qualitative sense of the turbulence structures that are captured. The improved spanwise resolution is evident in the WM_B1 figure. In front of the shock, the curves from WM_B2 & WM_B5 sit on top of each other and so do those from WM_B3 & WM_B4. This observation indicates that the leading edge streamwise spacing is to blame for the different results. Evidently, sufficient resolution in all three coordinate directions is necessary for obtaining the correct friction coefficient.

Table 4   Shock characteristics of the Type B meshes. Unlike Table (2), the lift and drag statistics are reported here as differences relative to WM_B1.

Case	Width of shock region (difference)	Mean shock location (difference)	$\langle C_L \rangle_t$ (difference)	$C_{L,\textbf{RMS}}$ (difference)	$\langle C_D \rangle_t$ (difference)	$C_{D,\textbf{RMS}}$ (difference)	Buffet frequency (St)
Experiment	0	0	-	-	-	-	0.0626
F&K WMLES	0.0720c	0.0435c	-	-	-	-	0.0644
WM_B1	0.0084c	0.0590c	0	0	0	0	0.0692 ± 0.0038
WM_B2	-0.0175c	0.0714c	0.0177	-0.0126	0.0007	-0.0010	0.0696 ± 0.0019
WM_B3	-0.0065c	0.0519c	-0.0377	-0.0072	-0.0017	-0.0007	0.0734 ± 0.0010
WM_B4	-0.0234c	0.0564c	-0.0130	-0.0152	-0.0005	-0.0014	0.0667 ± 0.0042
WM_B5	-	-	-0.0161	-0.0043	-0.0008	-0.0002	0.0776 ± 0.0043

B. Domain size sensitivity

To assess the impact of domain size on our simulations, we varied two key parameters using the WM_B2 mesh (approximately 234 million grid points) as our baseline due to computational constraints. First, we doubled the spanwise extent of the domain from $0.065c$ to $0.13c$ while maintaining consistent spanwise grid spacing, thereby doubling the number of spanwise grid points, resulting in a mesh with 469 million points. Second, we extended the farfield boundary from 80 chord lengths to approximately 200 by hyperbolically marching the existing grid blocks outward from the airfoil, increasing the grid point count to 242 million. These modifications allow us to evaluate the sensitivity of our results to both spanwise domain size and farfield extent, which are crucial factors in accurately capturing the flow physics,
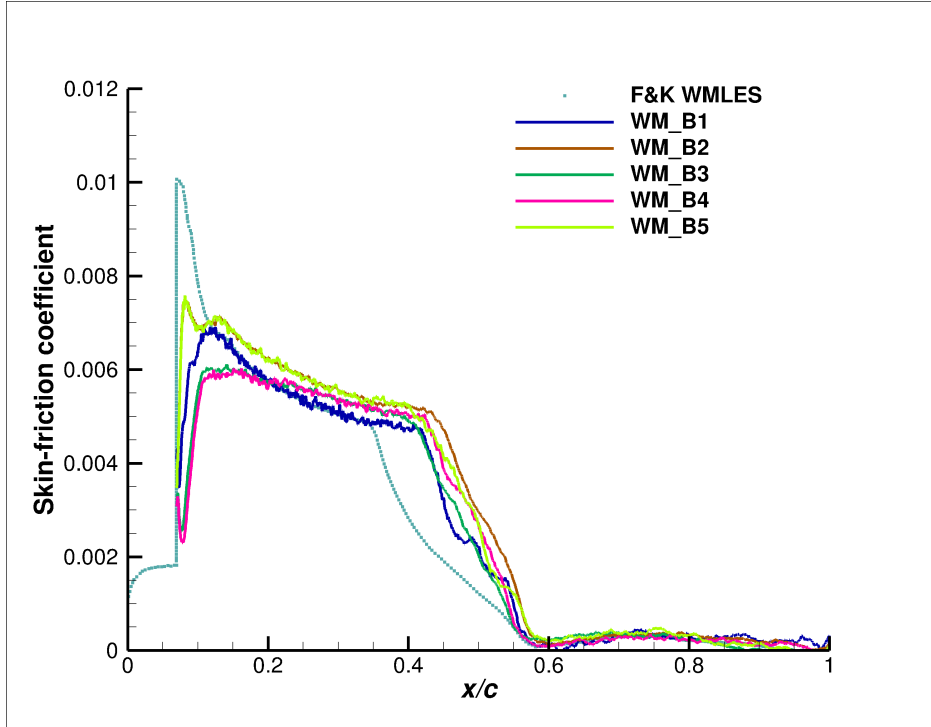
Fig. 11 Average skin-friction coefficient

particularly for phenomena like transonic buffet. It is clear that extending the domain in span had a greater impact on C_L and C_D than extending it in the far-field. To quantify the impact of each, we compute the relative change in the time-averaged C_L and its RMS value in Table (5). The results indicate that changing the farfield dimension had a negligible effect on these quantities, suggesting that our original domain boundary of $80c$ is sufficient for capturing the relevant flow features. However, doubling the spanwise extent resulted in changes in the C_L and C_D characteristics that are comparable to those observed when altering mesh resolution. This finding is particularly noteworthy as it suggests the presence of large-scale turbulence structures that may be on the order of the original spanwise extent, at least when using the convective flux discretization chosen for this study. Consequently, these structures may be unphysically confined when using a spanwise length of $0.065c$, potentially affecting the accuracy of our simulations.

Furthermore, extending the spanwise extent of the domain did not greatly affect the mean shock location, but it did have a noticeable effect on the size of the shock region itself (which is $0.0506c$ smaller than the experiment compared to $0.0175c$ smaller for WM_B2). These quantities are captured in Table (5). Similarly, the larger spanwise domain incurred a substantially larger RMSE in the shock region in terms of surface C_p: 0.3361 compared to 0.2721 for WM_B2 (see Table (6)).

It is important to note that conclusions about spanwise extent should be interpreted with caution, given the relatively short time-history of the simulation. The extended domain case ran for approximately 2.5 buffet cycles after initial transients were convected out of the domain (39 CTUs). However, this averaging window is consistent with previous studies, such as Fukushima et al. [11], who used a time record of 30 convective time units for computing statistics. When considering these results, it is crucial to balance the potential improvements in accuracy against the significant increase in computational cost. The spanwise extended mesh, with its 469 million grid points, represents a substantial increase in computational requirements compared to the baseline WM_B2 mesh (234 million points) and the farfield extended mesh (242 million points). If computational resources are limited, researchers may need to carefully weigh the benefits of increased spanwise extent against the additional computational burden. In some cases, it may be possible to achieve acceptable results with the smaller domain size, particularly if the focus is on specific flow features rather than capturing all large-scale turbulent structures. These results underscore the importance of carefully considering domain size, particularly in the spanwise direction, when simulating complex flow phenomena like transonic buffet. Future studies may benefit from further investigation into the optimal spanwise extent and its impact on the accuracy and reliability of WMLES simulations in this flow regime, while also taking into account the associated computational costs.
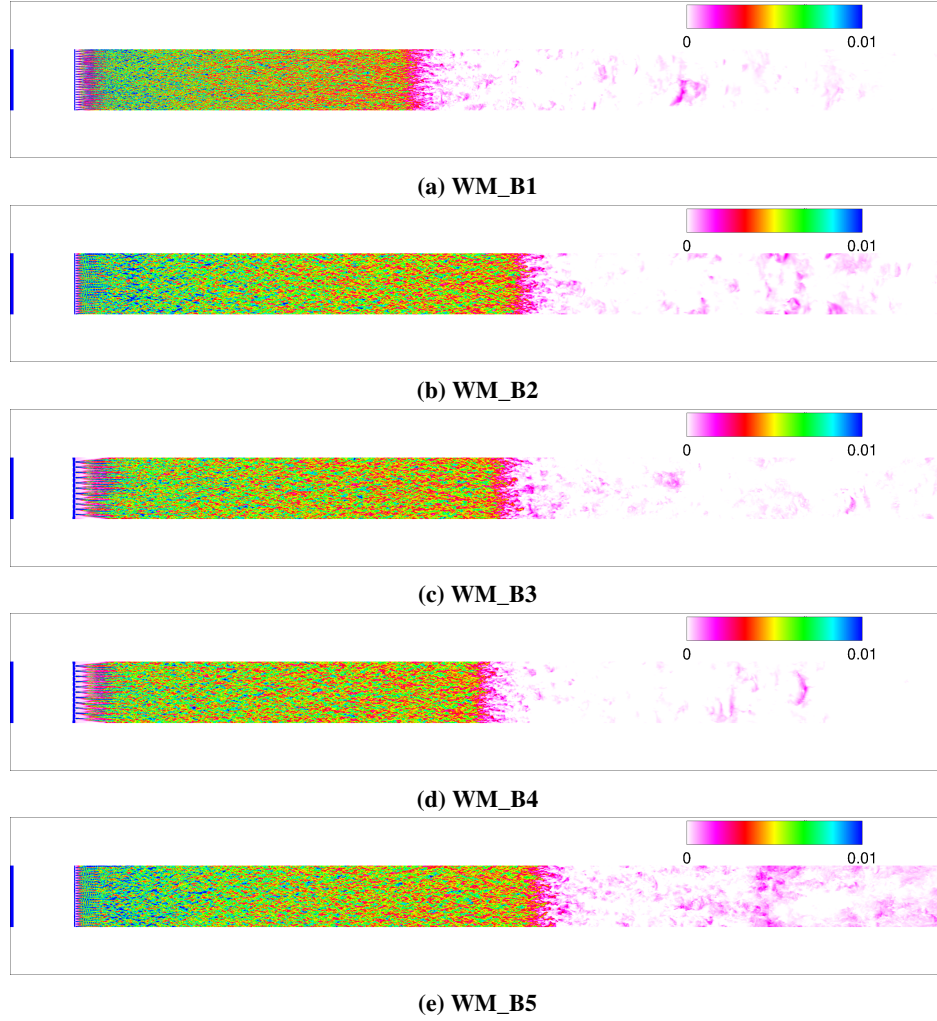
14

(a) WM_B1

(b) WM_B2

(c) WM_B3

(d) WM_B4

(e) WM_B5

Fig. 12   Instantaneous skin friction coefficient, C_{fx}.

Table 5   Shock characteristics for different domain sizes using the WM_B2 mesh distribution. WM_B2s2 doubles the spanwise extent of WM_B2 and WM_B2f2 extends the far field boundary from $80c$ to $200c$. As in similar tables above, shock width and mean location are reported relative to the experimental values. The difference in lift and drag statistics are relative to WM_B2 to show the sensitivity to domain size.

Case	Width of shock region (difference)	Mean shock location (difference)	$\langle C_L \rangle_t$ (difference)	$C_{L,\mathbf{RMS}}$ (difference)	$\langle C_D \rangle_t$ (difference)	$C_{D,\mathbf{RMS}}$ (difference)	Buffet frequency (St)
Experiment	0	0	-	-	-	-	0.0626
WM_B2	-0.0175c	0.0714c	0	0	0	0	0.0696 ± 0.0019
WM_B2s2	-0.0506c	0.0792c	-0.0215	0.0169	-0.0012	0.0013	0.0750 ± 0.0125
WM_B2f2	-0.0311c	0.0740c	-0.0007	0.0069	0.0001	0.0006	0.0690 ± 0.0043

15

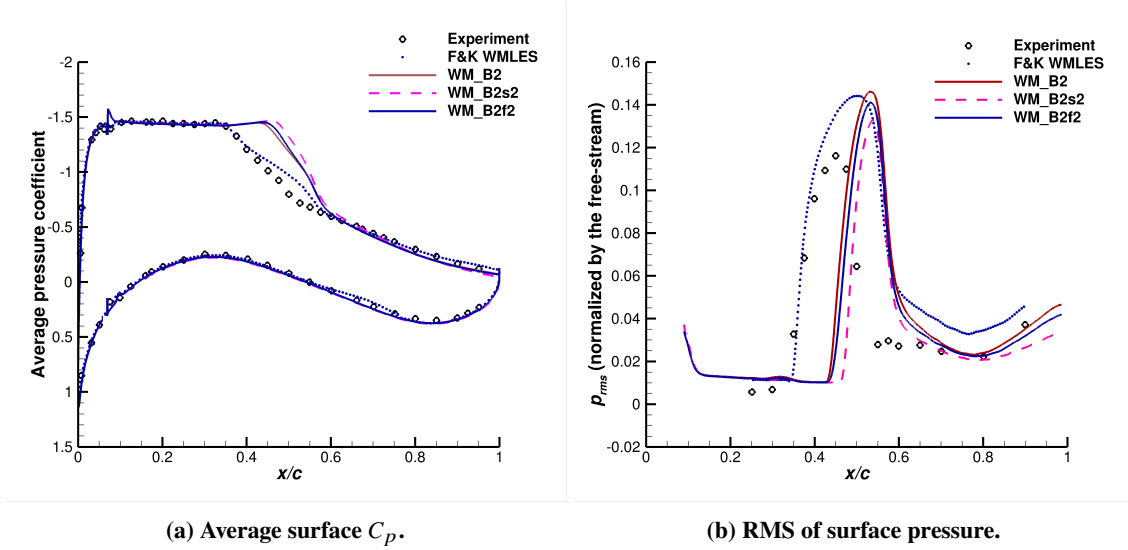(a) Average surface C_p.

(b) RMS of surface pressure.

Fig. 13 Surface pressure sensitivity to domain-size. B2s2 extends the spanwise domain by factor of 2. B2f2 extends the far-field boundary from 80c to 200c.

Table 6 RMSE of the suction-side surface pressure relative to the experimental data.

Case	Average C_p			Surface p_{RMS}		
	pre-shock	post-shock	shock region	pre-shock	post-shock	shock region
F&K WMLES	0.0007	0.0022	0.0697	0.0038	0.0138	0.0367
WM_B2	0.0139	0.0281	0.2721	0.0050	0.0069	0.0730
WM_B2s2	0.0109	0.0311	0.3361	0.0044	0.0044	0.0736
WM_B2f2	0.0143	0.0311	0.2889	0.0046	0.0054	0.0722

(a) Average surface C_p.
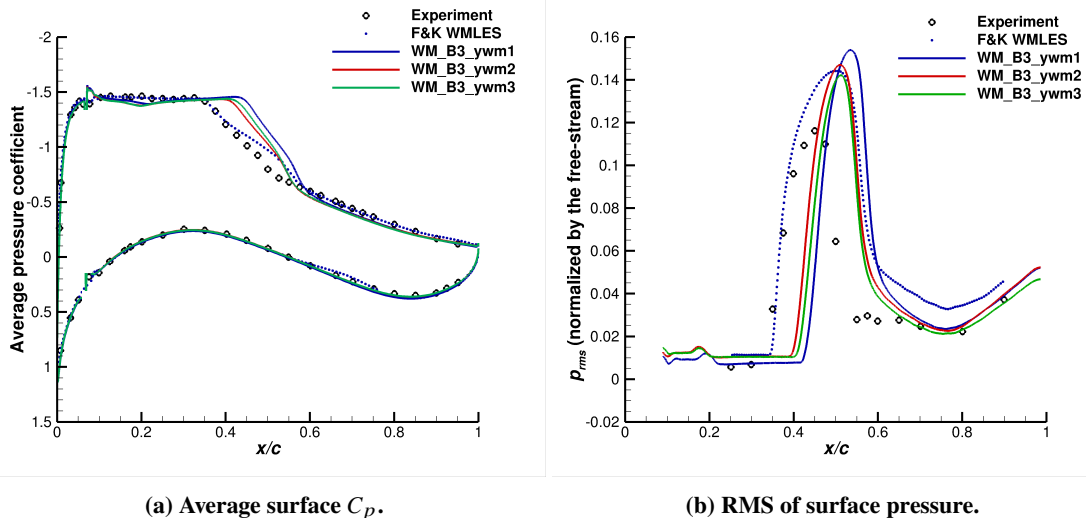(b) RMS of surface pressure.

Fig. 14   Surface pressure sensitivity to wall-model matching location.

C. Wall-model matching location

As noted previously, there are significant differences in the surface pressure coefficient as well as integrated quantities between our LAVA CFD solution and that of [11] using the same mesh. There are many possible differences between two numerical approaches, but it seems logical to begin with the closure models used in the implementation. We only consider the wall-model in this paper as we assume the inaccuracies near the wall are more important in terms of bulk quantities than subgrid errors away from the wall. Though, a complete analysis of the problem should include a detailed investigation of SGS model sensitivity and is part of our ongoing analysis.

Both our simulations and that of [11] utilize the equilibrium formulation of the wall model. There are two key differences between our model and that of Fukushima et al.: 1.) Our model is in algebraic form using a version of Musker's wall-function [46] modified for more computationally efficient evaluations (unpublished), whereas Fukushima and Kawai [11] solve the full ODE system arising from equilibrium assumptions and 2.) Our wall-model matching location is fixed at the second off-wall grid point whereas [11] used the fifth point based on physical arguments regarding the resolution of turbulence structures in the boundary layer. We suspect that the former is inconsequential since both the ODE and algebraic formulations result in the same analytical mean velocity profile.

According to [11], using the fifth off-wall point (at the given resolution) to match the wall-model and LES solutions allows for adequate resolution of turbulence structures that are on the order of the matching height. Fukushima et al. argue that a matching location closer to the wall would utilize data which cannot be accurate due to under-resolved energetic turbulence structures at that location. Currently, our software allows the wall-model to use LES velocity data exclusively at the first, second, or third off-wall grid points. Further software development will be necessary to enable matching locations beyond the third off-wall grid point. The coarsest Type B mesh (WM_B3) was chosen to perform this study, as it had the overall lowest simulation cost compared to the other Type B meshes. Another benefit of the WM_B3 mesh is that due to its coarser wall-normal spacing, our third off-wall matching location is more closely aligned with Fukushima's fifth matching location in non-dimensional grid units. Table (7) demonstrates the sensitivity of the integrated lift and drag to the choice of matching location, whereas Fig. (14) illustrates the variation in surface pressure signals across the three cases which is further quantified in Table (8). These variations are similar in magnitude to the changes seen when varying mesh resolution. Larger differences are observed between utilizing the first off-wall point and the second off-wall point as the matching location, compared to the differences observed between the second and third off-wall points. This implies that as the matching location is increased, the sensitivity in time-averaged surface and integrated quantities decreases. These findings highlight the importance of carefully selecting the wall-model matching location and its potential impact on the accuracy of both surface pressure and integrated quantity predictions. While the differences observed are significant, further investigation is needed to fully understand the underlying mechanisms and establish best practices for wall-model matching location height in WMLES simulations of transonic buffet.

17

Table 7 Shock characteristics for different wall model matching locations. The lift and drag statistics are reported as the difference from WM_B3 using the second off-wall mesh point to match the wall model and LES solution. The second off-wall grid point was used in all other WMLES cases we ran and so this is used as the "baseline" for the present comparison.

Case	Width of shock region (difference)	Mean shock location (difference)	$\langle C_L \rangle_t$ (difference)	$C_{L,\textbf{RMS}}$ (difference)	$\langle C_D \rangle_t$ (difference)	$C_{D,\textbf{RMS}}$ (difference)	Buffet frequency (St)
Experiment	0	0	-	-	-	-	0.0626
WM_B3 (1st point)	-0.0156c	0.0746c	0.0425	-0.0005	0.0009	0.0002	0.0750 ± 0.0042
WM_B3 (2nd point)	-0.0065c	0.0519c	0	0	0	0	0.0734 ± 0.0010
WM_B3 (3rd point)	-0.0227c	0.0526c	0.0030	-0.0082	0.0001	-0.0007	0.0775 ± 0.0039

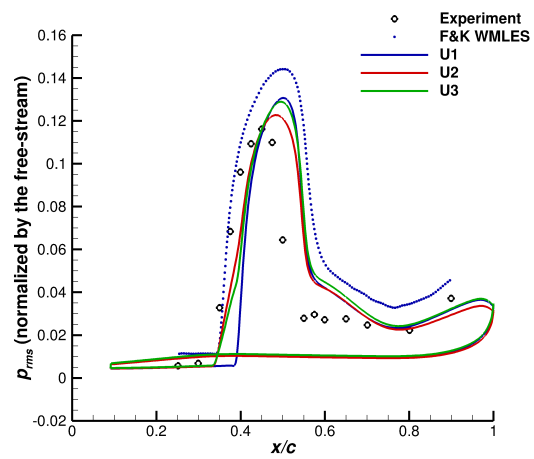**Table 8 RMSE of the suction-side surface pressure relative to the experimental data.**

Case	Average C_p			Surface $p_{\textbf{RMS}}$		
	pre-shock	post-shock	shock region	pre-shock	post-shock	shock region
WM_B3 (1st point)	0.0347	0.0350	0.2588	0.0015	0.0072	0.0769
WM_B3 (2nd point)	0.0483	0.0434	0.1701	0.0033	0.0052	0.0590
WM_B3 (3rd point)	0.0486	0.0450	0.2001	0.0033	0.0032	0.0594

Table 9 Shock characteristics for URANS and HRLES. The shock width and mean shock location were not reported for H1 because the metrics we've chosen don't give meaningful results for this case (due to the fact that $p_{\textbf{RMS}}$ is above 40% of its maximum the entire aft end of the airfoil).

| Case	Width of shock region (difference)	Mean shock location (difference)	$\langle C_L \rangle_t$	$C_{L,\textbf{RMS}}$	$\langle C_D \rangle_t$	$C_{D,\textbf{RMS}}$	Buffet frequency (St)
Experiment	0	0	-	-	-	-	0.0626
WM_B1	0.0084c	0.0590c	0.9762	0.0822	0.0471	0.0072	0.0692 ± 0.0038
U1	0.0058c	0.0415c	0.9484	0.0747	0.0452	0.0066	0.0639 ± 0.0006
U2	0.0279c	0.0240c	0.9438	0.0753	0.0453	0.0064	0.0615 ± 0.0015
U3	0.0195c	0.0363c	0.9450	0.0801	0.0451	0.0070	0.0633 ± 0.0017
H1	-	-	1.0116	0.0218	0.0510	0.0032	0.0922 ± 0.0010
H2	-0.0714c	-0.0448c	0.9965	0.0292	0.0527	0.0040	0.0949 ± 0.0017
H3	0.0175c	-0.0240c	0.9891	0.0713	0.0511	0.0075	0.0800 ± 0.0017
H3b	-0.0013c	-0.0253c	0.9906	0.0610	0.0508	0.0063	0.0833 ± 0.0017
H4	-0.0201c	-0.0182c	0.9995	0.0542	0.0513	0.0056	0.0800 ± 0.0017
H4b	0.0188c	0.0156c	0.9978	0.0723	0.0493	0.0069	0.0767 ± 0.0017
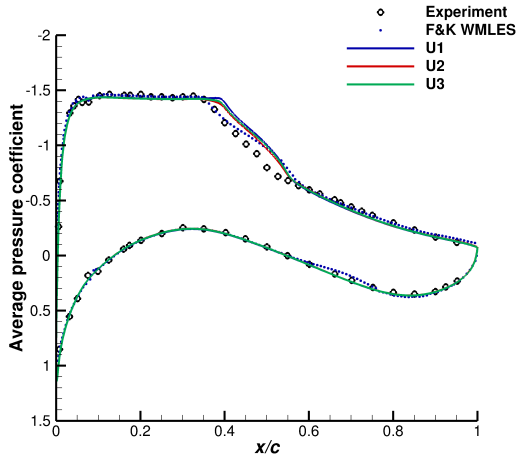
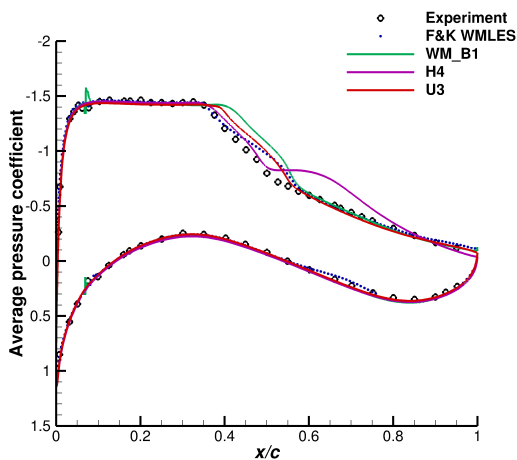(a) Average surface C_p for the URANS cases.

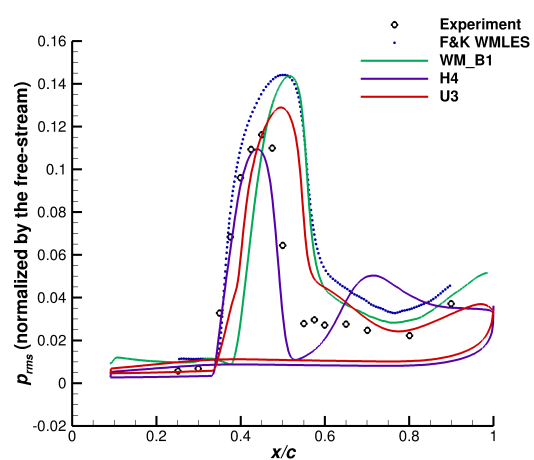(b) RMS of surface pressure for the URANS cases.
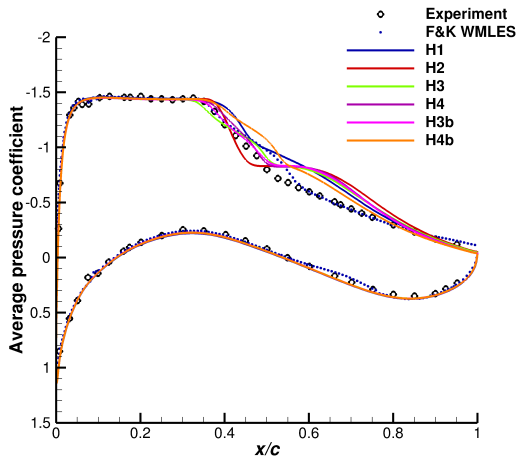
(c) Average surface C_p for the HRLES cases.
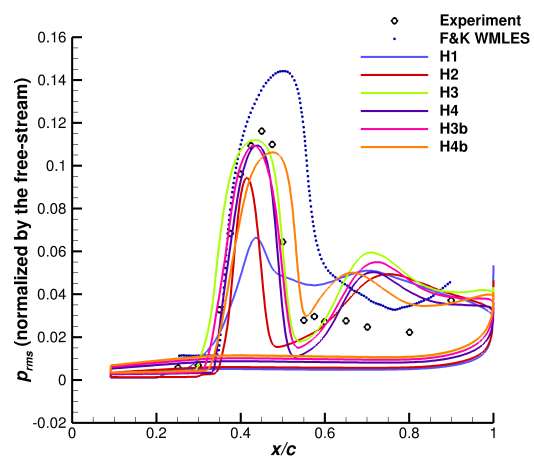
(d) RMS of surface pressure for the HRLES cases.

(e) Average surface C_p comparison between URANS, HRLES, and WMLES.

(f) RMS of surface pressure comparison between URANS, HRLES, and WMLES.

Fig. 15   Surface pressure comparison for URANS, HRLES, and WMLES

Table 10   RMSE of the suction-side surface pressure relative to the experimental data.

Case	Average C_p			Surface $p_{\mathbf{RMS}}$		
	pre-shock	post-shock	shock region	pre-shock	post-shock	shock region
F&K WMLES	0.0007	0.0022	0.0696	0.0038	0.0138	0.0367
WM_B1	0.0219	0.0112	0.1905	0.0030	0.0082	0.0581
U1	0.0224	0.0249	0.1356	0.0027	0.0056	0.0468
U2	0.0246	0.0224	0.1050	0.0027	0.0058	0.0340
U3	0.0243	0.0218	0.1203	0.0025	0.0071	0.0403
H1	0.0078	0.1023	0.1609	0.0023	0.0217	0.0340
H2	0.0104	0.1519	0.1105	0.0058	0.0191	0.0403
H3	0.0129	0.1196	0.1073	0.0049	0.0249	0.0146
H4	0.0095	0.1328	0.1039	0.0046	0.0177	0.0162
H3b	0.0117	0.1269	0.1008	0.0031	0.0217	0.0112
H4b	0.0095	0.0736	0.1699	0.0036	0.0171	0.0201

Table 11   Comparison of computational costs. Each column pair shows Case and CPU-hours per CTU.

URANS		HRLES		WMLES	
U1	46.20	H1	61.02	WM_A	6,702.22
U2	182.00	H2	164.53	WM_B1	11,427.41
U3	692.57	H3	515.11	WM_B2	4,771.87
		H4	3,066.73	WM_B3	3,300.42
		H3b	605.66	WM_B4	2,553.19
		H4b	3,979.34	WM_B5	6,567.60
				WM_B2s2	8,653.15
				WM_B2f2	4,782.35

D. Comparison of WMLES with URANS and HRLES

One of the unique aspects of this study is our ability to compare URANS, HRLES, and WMLES approaches within the same solver framework using consistent numerics. This allows us to directly assess the differences in shock buffet predictions across these solution paradigms, which span a range of turbulence closure models and computational costs. To the best of our knowledge, this is the first time a single solver has been used to conduct such a comparative analysis of URANS, HRLES, and WMLES specifically for transonic shock buffet phenomena. By leveraging the versatility of our in-house LAVA solver, we can isolate the impact of the turbulence modeling approach while maintaining consistency in other numerical aspects, providing valuable insights into the relative merits and limitations of each method for this challenging flow problem.

We ran a series of unsteady RANS simulations and HRLES varying the mesh resolution (see Section III.C). A fixed time-step of 100 steps per CTU was used for all URANS simulations, while the time-step was reduced from the URANS levels by factors of two with increasing mesh resolution for the HRLES. Both methods used an implicit BDF2 time-discretization embedded within a dual-time framework, and sub-iterations were performed at each time-step until $3-4$ orders of magnitude of residual reduction was achieved. The quantified difference in lift and drag between the Type B meshes is similar across the URANS and HRLES cases, with the notable exception of cases H1 and H2, which apparently are too coarse to capture the relevant physics (see Table (9)). One notable observation on the HRLES cases is the persistent "bump" in surface C_p post-shock (Fig. (15c)). We suspect this is due to insufficient resolution of the shear layer at the edge of the separated boundary layer. Notably, our URANS result gives the best agreement with the experiment and is relatively insensitive to mesh resolution.

Based on the close correspondence between URANS and experiment, and the lack of agreement with our WMLES, it begs the question of how expensive are our WMLES compared to the URANS and HRLES runs. We computed the number of CPU-hours required to simulate one convective time unit and reported the result in Table (11). The highest resolution URANS simulation is 6% the cost of WM_B1, which performed the best amongst our WMLES meshes. We draw two conclusions from this cost-comparison: 1.) URANS is a viable and affordable strategy for this problem (in terms of the quantities reported here), and 2.) Before running a WMLES of an aerodynamic system in the buffet regime, one must be careful in developing the mesh and deciding on particular wall-model settings and numerics because the cost is significant and, as we have seen, simply using WMLES and a high-resolution mesh does not guarantee a reliable answer.

V. Conclusion

A number of sensitivity studies utilizing WMLES of flow over the ONERA OAT15A airfoil at a known buffet condition were performed resulting in the current findings:

1) When holding the near-wall mesh resolution constant, significant sensitivity between the Type A and Type B meshes was observed in both integrated loads as well as time-averaged surface quantities. Previously, the Type A mesh was established as the best-practice when generating large overset grids for complex geometries such as the full CRM aircraft in [12]. However, following this practice on a "simple" geometry when large, oscillating shocks are present, poor prediction of large-scale quantities such as C_L and C_p were the result. Conversely, the Type B mesh performed much better in terms of these quantities. There are two main differences between the two meshes. First, there is significantly more stream-wise resolution above the airfoil in the shock region. And second, there is more resolution throughout the wake region behind the airfoil. Whether one or both of these are the critical factor remains to be determined and should be explored in future studies. However, practicing engineers attempting to simulate problems where shock buffet is present should consider the appropriate grid resolution over the shock region away from the body and the suction side of the wing as a whole.

2) The finest resolution case (WM_B1) performed the best, but coarsening in the span and wall-normal directions (WM_B2) resulted in comparable performance in terms of C_L, C_D, C_p, and p_{rms}. The spanwise and wall-normal spacing has a greater impact on the predicted skin friction. As noted previously, the particular value of the near-wall spacings for the high-resolution mesh were physically motivated based on boundary layer thickness as established in Kawai and Larsson [42]. Therefore, other than WM_B1, all Type B cases violate the considerations in that paper, but we do see reliable predictions (relative to the high resolution case) when relaxing these constraints.

3) Of the quantities considered in this paper, doubling the span-wise extent of the domain had as much of an effect as changes in the mesh resolution. However, the effects were significantly less than changes in the mesh distribution (i.e., between Type A and Type B meshes). A more detailed look at two-point correlations should be done to

quantify the level of confinement of the large spanwise structures in the two domains. In terms of far-field extent, we saw negligible sensitivity between the two runs and therefore conclude that a far-field boundary $80c$ from the airfoil is sufficient.

4) We did see sensitivity to wall-model matching when comparing between the first and second off-wall points. It is reasonable to suspect that changes may persist to even higher matching locations. It is important to keep in mind that the optimal matching location is in the log-layer region of the boundary layer, but as Kawai and Larsson [42] argue, it may also be important to have well-resolved turbulent structures at the matching location. Therefore, it is critical when building a mesh that these ideas be taken into consideration before blindly applying WMLES to a given problem.

The results from the present study do not constitute an exhaustive list of best-practices when using WMLES to simulate shock-buffet problems. Rather, they are the beginning of an ongoing study. Future work includes a detailed modal analysis of the flow field to determine the sensitivity of isolated "modes" to mesh resolution and domain size. Additionally, we plan to implement further wall-matching locations in our code to provide a closer comparison between our WMLES and the results in [11]. Furthermore, it will be beneficial to assess the sensitivity to the shock-capturing scheme and choice of shock-sensor and its associated threshold, as these will likely have significant influence over the shock dynamics.

References

[1] Hilton, W. F., and Fowler, R., "Photographs of shock wave movement," *NPL R & M No. 2692, National Physical Laboratories*, 1947.

[2] Giannelis, N. F., Vio, G. A., and Levinski, O., "A review of recent developments in the understanding of transonic shock buffet," *Progress in Aerospace Sciences*, Vol. 92, 2017, pp. 39–84.

[3] Barakos, G., and Drikakis, D., "Numerical simulation of transonic buffet flows using various turbulence closures," *International Journal of Heat and Fluid Flow*, Vol. 21, No. 5, 2000, pp. 620–626.

[4] Goncalves, E., Robinet, J.-C., and Houdeville, R., "Numerical simulation of transonic buffet over an airfoil," *Third Symposium on Turbulence and Shear Flow Phenomena*, Begel House Inc., 2003.

[5] Goncalves, E., and Houdeville, R., "Turbulence model and numerical scheme assessment for buffet computations," *International Journal for Numerical Methods in Fluids*, Vol. 46, No. 11, 2004, pp. 1127–1152.

[6] Illi, S., Lutz, T., and Krämer, E., "On the capability of unsteady RANS to predict transonic buffet," *Third Symposium Simulation of Wing and Nacelle Stall*, 2012, pp. 21–22.

[7] Choi, H., and Moin, P., "Grid-point requirements for large eddy simulation: Chapman's estimates revisited," *Physics of fluids*, Vol. 24, No. 1, 2012.

[8] Deck, S., "Numerical simulation of transonic buffet over a supercritical airfoil," *AIAA journal*, Vol. 43, No. 7, 2005, pp. 1556–1566.

[9] Garnier, E., and Deck, S., "Large-eddy simulation of transonic buffet over a supercritical airfoil," *Direct and Large-Eddy Simulation VII: Proceedings of the Seventh International ERCOFTAC Workshop on Direct and Large-Eddy Simulation, held at the University of Trieste, September 8-10, 2008*, Springer, 2010, pp. 549–554.

[10] Grossi, F., Braza, M., and Hoarau, Y., "Prediction of transonic buffet by delayed detached-eddy simulation," *AIAA Journal*, Vol. 52, No. 10, 2014, pp. 2300–2312.

[11] Fukushima, Y., and Kawai, S., "Wall-modeled large-eddy simulation of transonic airfoil buffet at high Reynolds number," *AIAA journal*, Vol. 56, No. 6, 2018, pp. 2372–2388.

[12] Ghate, A. S., Kenway, G. K., Stich, G.-D., Browne, O. M., Housman, J. A., and Kiris, C. C., "Transonic lift and drag predictions using wall-modelled large eddy simulations," *AIAA Scitech 2021 Forum*, 2021, p. 1439.

[13] Goc, K., Agrawal, R., Moin, P., and Bose, S., "Studies of transonic aircraft flows and prediction of initial buffet onset using large-eddy simulations," *AIAA Aviation 2023 Forum*, 2023, p. 4338.

[14] Tamaki, Y., and Kawai, S., "Wall-modeled LES of transonic buffet over NASA-CRM using Cartesian-grid-based flow solver FFVHC-ACE," *AIAA SciTech 2023 Forum*, 2023, p. 16.

[15] Kiris, C., Housman, J., Barad, M., Brehm, C., Sozer, E., and Moini-Yekta, S., "Computational Framework for Launch, Ascent, and Vehicle Aerodynamics (LAVA)," *Aerospace Science and Technology*, Vol. 55, 2016, pp. 189–219.

[16] Gottlieb, S., and Shu, C.-W., "Total variation diminishing Runge-Kutta schemes," *Mathematics of computation*, Vol. 67, No. 221, 1998, pp. 73–85.

[17] Steger, J., and Benek, J., "On the Use of Composite Grid Schemes in Computational Aerodynamics," Technical Memorandum 88372, NASA, 1986.

[18] Stich, G.-D., Housman, J., Kocheemoolayil, J., Barad, M., and Kiris, C., "Application of Lattice Boltzmann and Navier-Stokes Methods to NASA's Wall Mounted Hump," *AIAA Aviation Forum, Atlanta, Georgia*, 2018.

[19] Housman, J., Stich, G., and Kiris, C., "Predictions of Slat Noise from the 30P30N at High Angles of Attack using Zonal Hybrid RANS-LES," *AIAA/CEAS Aeroacoustics Conference*, 2019.

[20] Ghate, A. S., Housman, J. A., Stich, G.-D., Kenway, G., and Kiris, C. C., "Scale Resolving Simulations of the NASA Juncture Flow Model using the LAVA Solver," *AIAA Aviation 2020 Forum*, 2020.

[21] Ghate, A. S., Kenway, G., Stich, G.-D., Browne, O., Housman, J., and Kiris, C. C., "Transonic lift and drag predictions using Wall-Modelled Large Eddy Simulations," *AIAA Scitech 2021 FORUM*, 2021.

[22] Brehm, C., Barad, M., Housman, J., and Kiris, C., "A Comparison of Higher-Order Finite-Difference Shock Capturing Schemes," *Computers & Fluids*, Vol. 122, 2015, pp. 184–208.

[23] Craig-Penner, D., Housman, J., Stich, G.-D., Koch, J. R., and Duensing, J., "Wall-Modeled Large-Eddy Simulations of a Swept Wing," *AIAA SciTech Forum, Orlando, Florida*, 2024. AIAA-2024-2376.

[24] Allmaras, S. R., and Johnson, F. T., "Modifications and clarifications for the implementation of the Spalart-Allmaras turbulence model," *Seventh international conference on computational fluid dynamics (ICCFD7)*, Vol. 1902, Big Island, HI, 2012.

[25] Deck, S., and Renard, N., "Towards an enhanced protection of attached boundary layers in hybrid RANS/LES methods," *Journal of Computational Physics*, Vol. 400, 2020, p. 108970.

[26] Koch, J. R., Dumlupinar, E., Housman, J. A., Kiris, C. C., Patel, M. M., Kleb, B., Brauckmann, G. J., and Alter, S. J., "CFD analysis of Space Launch System solid rocket booster separation within the Langley Unitary Plan Wind Tunnel," *AIAA Aviation 2021 Forum*, 2021, p. 2966.

[27] Piomelli, U., and Balaras, E., "Wall-layer models for large-eddy simulations," *Annual Review of Fluid Mechanics*, Vol. 34, No. 1, 2002, pp. 349–374.

[28] Larsson, J., Kawai, S., Bodart, J., and Bermejo-Moreno, I., "Large Eddy Simulation with Modeled Wall-Stress: Recent Progress and Future Directions," *J-STAGE*, 2015.

[29] Bose, S., and Park, G., "Wall-Modeled Large-Eddy Simulation for Complex Turbulent Flows," *Annual Review of Fluid Mechanics*, Vol. 50, 2018, pp. 535–561.

[30] Ghate, A. S., Kenway, G. K., Stich, G.-D., Browne, O. M., Housman, J. A., and Kiris, C. C., "Transonic lift and drag predictions using wall-modelled large eddy simulations," *AIAA SCITECH 2021 Forum*, American Institute of Aeronautics and Astronautics, 2021. AIAA Paper 2021-1439.

[31] Ghate, A. S., Stich, G.-D., Kenway, G. K., Housman, J. A., and Kiris, C. C., "A wall-modeled LES perspective for the high lift common research model using LAVA," *AIAA AVIATION 2022 Forum*, American Institute of Aeronautics and Astronautics, 2022. AIAA Paper 2022-3434.

[32] Wong, M. L., Kenway, G. K., Ghate, A. S., Stich, G.-D., and Kiris, C. C., "Predictions of LAGOON nose landing gear flow and noise using wall-modeled large eddy simulations," *28th AIAA/CEAS Aeroacoustics 2022 Conference*, American Institute of Aeronautics and Astronautics, 2022. AIAA Paper 2022-2850.

[33] Wong, M. L., Ghate, A. S., Stich, G.-D., Kenway, G. K., and Kiris, C. C., "Numerical study on the aerodynamics of an iced airfoil with scale-resolving simulations," *AIAA SCITECH 2023 Forum*, American Institute of Aeronautics and Astronautics, 2023. AIAA Paper 2023-0252.

[34] Kiris, C. C., Ghate, A. S., Duensing, J. C., Browne, O. M. F., Housman, J. A., Stich, G.-D., Kenway, G. K., Fernandes, L. S., and Machado, L. M., "High-lift common research model: RANS, HRLES, and WMLES perspectives for CLmax prediction using LAVA," *AIAA SCITECH 2022 Forum*, American Institute of Aeronautics and Astronautics, 2022. AIAA Paper 2022-1554.

[35] "Pointwise: Mesh Generation Software for CFD," https://www.pointwise.com/, 2024. Accessed: June 26, 2024.

[36] Chan, W., "Developments in Strategies and Software Tools for Overset Structured Grid Generation and Connectivity," *20th AIAA Computational Fluid Dynamics Conference, Honolulu, Hawaii*, 2011. AIAA-2011-3051.

[37] Maldonado, D., Housman, J., Dumlupinar, E., Stich, G. D., Duensing, J., and Milholen, W., "Evaluation of a Physics-Based Unsteady RANS Method for Buffet Onset Prediction," *AIAA AVIATION 2024 Forum*, July2024. https://doi.org/10.2514/6.2016-3690.

[38] Jensen, J. C., Stich, G.-D., Housman, J. A., Denison, M., and Kiris, C. C., "Lava simulations for the 3rd aiaa cfd high lift prediction workshop using body fitted grids," *2018 AIAA Aerospace Sciences Meeting*, 2018, p. 2056.

[39] Stich, G.-D., Fernandes, L. S., Duensing, J. C., Housman, J. A., Kenway, G. K., and Kiris, C. C., "Validation of Actuator Disk, Actuator Line and Sliding Mesh Methods within the LAVA Solver," *The 11th International Conference on Computational Fluid Dynamics*, 2022.

[40] Kiris, C. C., Ghate, A. S., Duensing, J. C., Browne, O. M., Housman, J. A., Stich, G.-D., Kenway, G., Fernandes, L. S., and Machado, L. M., "High-lift common research model: RANS, HRLES, and WMLES perspectives for CLmax prediction using LAVA," *AIAA SciTech 2022 Forum*, 2022, p. 1554.

[41] Stich, G.-D., Martin, O. G., Ashby, C., Housman, J. A., and Duensing, J., "Noise Prediction of Multi-Stream Internally Mixed Jets With External and Internal Pligs Using Large-Eddy Simulation," *30th AIAA/CEAS Aeroacoustics Conference (2024)*, 2024, p. 3377.

[42] Kawai, S., and Larsson, J., "Wall-modeling in large eddy simulation: Length scales, grid resolution, and accuracy," *Physics of fluids*, Vol. 24, No. 1, 2012.

[43] Jacquin, L., Molton, P., Deck, S., Maury, B., and Soulevant, D., "Experimental study of shock oscillation over a transonic supercritical profile," *AIAA journal*, Vol. 47, No. 9, 2009, pp. 1985–1994.

[44] Crouch, J., Garbaruk, A., Magidov, D., and Travin, A., "Origin of transonic buffet on aerofoils," *Journal of Fluid Mechanics*, Vol. 628, 2009, pp. 357–369.

[45] Browne, O. M., Maldonado, D., Housman, J. A., Duensing, J. C., and Milholen, W. E., "Predicting Transonic Buffet Onset for the Boeing Transonic Truss-Braced Wing Aircraft," *Accepted for Publication in Journal of Aircraft*, Vol. XX, No. X, 202X, pp. XXXX–XXXX.

[46] Musker, A., "Explicit expression for the smooth wall velocity distribution in a turbulent boundary layer," *AIAA Journal*, Vol. 17, No. 6, 1979, pp. 655–657.